The Surface Structure and Corrosion Resistance of ZrO$_2$-Doped Silane Film on Cold-Rolled Steels

Xingrui Zheng[1], Jiyi Li[1], Hao Yang[1], Yiqi Cui[2,3,]*

[1] City college, Kunming University of Science and Technology, Kunming 650093, China;
[2] Faculty of Land Resource Engineering, Kunming University of Science and Technology, Kunming 650093, China;
[3] Yunnan Province Engineering Research Center for Reutilization of Metal Tailings Resources, Kunming 650093, China.
[*]E-mail: kmust_cyq@163.com

A novel green fluorozirconic acid-based conversion film on cold-rolled steels was proposed in this work. Various methods were used to determine the surface structure and the corrosion behavior of the film. Compared with the corrosion current of the silane film, the corrosion current of this film was reduced by 10% and the film provided satisfactory corrosion resistance in 5% NaCl solution. In addition, the stability of the conversion film was 38.5% higher than that of the silane film. This resulted from a Si-O-Zr bond, formed between the materials and the metal matrix, which yielded considerable improvement in the corrosion resistance of the cold-rolled steels. Therefore, this study constitutes a clear advance in the properties of conversion films on cold-rolled steels.

1. INTRODUCTION

Cold-rolled steel has been widely used in many applications including aviation, machinery manufacturing, vehicle engineering, shipping and marine projects as well as bridge and building engineering [1–4]. However, the wide application of these steels has been severely limited by their poor corrosion behavior [5–8]. Therefore, the development of a protective film is essential for improving the corrosion resistance of these steels.

Silane surface technology has been rapidly developed due to its simple synthesis of raw materials as well as green and pollution-free characteristics [9–12]. Through the barrier effect, a silane film can prevent contact between the corrosive medium and the metal matrix, thereby improving the corrosion resistance of the metal in aggressive environments [13–15]. However, the monolayer silane

film is unstable and exhibits poor corrosion resistance and, hence, improvement of the film anti-corrosion performance is essential. Conventional methods of improving this performance include doping the material with nano-SiO_2, CeO_2 and ZnO. These doping modifications improve the anti-corrosion properties and exploit the advantages and characteristics of the doping elements [16–19].

Although Zr exhibits strong corrosion resistance and occurs abundantly in the earth's crust, Zr-doped silane films have rarely been used to protect metals from corrosion [20–24]. Herein, we report a Zr-salt-doped composite silane film prepared by means of a sol-gel method using sodium fluorozirconate and 1,2-Bis (trimethoxysilyl) ethane (BTMSE) as precursors [25–26]. The surface structure and corrosion behavior of the doped modified film were investigated.

2. MATERIALS AND METHODS

2.1 Materials

A 80 mm × 20 mm × 2 mm substrate fabricated from cold-rolled steel plate Q235 (Alibaba, Shanghai) was employed. In addition, 1,2-Bis (trimethoxysilyl) ethane (BTMSE), sodium fluorozirconate (AR), and methanol (AR) were purchased from Nanjing Chemical Reagent Co., Ltd.

2.2 Experimental Design and Statistical

Prior to preparation of the film layer, cold-rolled steel plate Q235 was sequentially polished with various grits (#400 to #1000) of silicon carbide paper. The plate was rinsed successively with water, acetone and deionized water, then dried. A 10 mm × 10 mm working electrode was fabricated from the plate and placed in a drying dish for use.

The silane sol solution was prepared from the following ratio of components, V(BTMSE): V(methanol): V (distilled water) - 5:15:80, with 0.01 mol/L nitric acid and ammonia water used to adjust the exact pH to 4.1. The mixture was magnetically stirred for 60 min in a closed vessel at room temperature, and then hydrolyzed for 24 h to obtain a monosilane sol solution.

The fluorozirconic-acid-silane composite sol solution was prepared using sodium fluorozirconate mixed with water and completely dissolved to obtain a 1×10^{-3} mol/L sodium fluorozirconate solution. The solution consisted of components in the following ratio V(BTMSE): V (methanol): V(zirconium salt solution)-5:15:80, with 0.01 mol/L nitric acid and ammonia water used to adjust the exact pH = 4.1. Subsequently, the mixture was magnetically stirred for 60 min in a closed vessel at room temperature, and the composite sol solution was obtained after aging for 24 h.

The film layer pretreat was prepared by immersing the sample in 0.10% (mass fraction, the same below) NaOH solution for 30 s at room temperature, then rinsing with deionized water. Afterward, the sample was completely wet with deionized water (to form a seamless water film), using the dipping method. The sample was then placed in a silanol solution and a silanol-doped Zr salt solution for 5 min, removed, dried with compressed air, placed in an oven, and dried at 150°C for 30 min.

In this work, blank samples without the film formation were referred to as sample 1. Film-forming samples treated with the silane solution and with the fluorozirconic acid-silane composite solution were referred to as sample 2 and sample 3, respectively.

2.2 Characterization and electrochemical measurements

The pH was measured using a PHS-3 precision acidity meter; the microstructure of the sample was observed via field emission scanning electron microscopy (S-4800FE) and the distribution of specific elements in the film was further analyzed by means of EDS. The film was also investigated via Fourier transform infrared spectroscopy (FTIR; Bruker Vector 33) and Axis Ultra DLD multifunctional X-ray photoelectron spectroscopy (XPS). Corrosion resistance tests were performed on a CHl660B electrochemical workstation. A three-electrode system was employed. A 3 mm × 3 mm sample, saturated calomel electrode, 10 mm × 10 mm platinum electrode, and 3.5% NaCl solution were used as the working electrode, reference electrode, auxiliary electrode, and corrosive medium, respectively. The scanning potential at the initial point of the potentiodynamic polarization curves was -1.0 V, the terminal potential was -0.2 V, and the scanning rate was -1 mV/s. The anodic polarization curve was obtained at a scan rate of 0.5 mV/s for potential ranging from -0.8 V to 0.2 V. The peak-to-peak fitting was performed using the Gauss/Laurent's equation minimum mean square error Shirley elimination background method. A scanning frequency ranging from 0.1 Hz to 10 kHz at 25°C was employed. The amplitude of the alternating current (AC) excitation signal was 1 mV/s, and the AC impedance was measured. The NaCl solution (mass fraction: 5%, pH: 7) was used for the soaking experiment. A type DCTC1200P salt spray corrosion test chamber was used to moderate the salt fog test. The aforementioned 5% NaCl solution was used as the corrosion liquid and the temperature in the cabinet was maintained at 35°C, for 15 h of continuous spraying.

3. RESULTS AND DISCUSSION

3.1 SEM and EDS Analysis

SEM micrographs with EDS element mapping of the samples are shown in Fig. 1. Many microscopic cracks and pores, resulting from the film stress [27] and dissolution-induced hydrogen [28], were observed in the surface of sample 1 (Fig. 1(a)) and sample 2 (Fig. 2(b)). The surface of sample 3 (Fig. 1(c)) was uniform and dense, the structure was relatively complete, and the cracks and pores observed were fewer than in the other samples. This suggested that the fluorozirconic acid-silane composite sol solution yielded a dense composite film on the surface of the sample and improved the coverage of the film on the substrate.
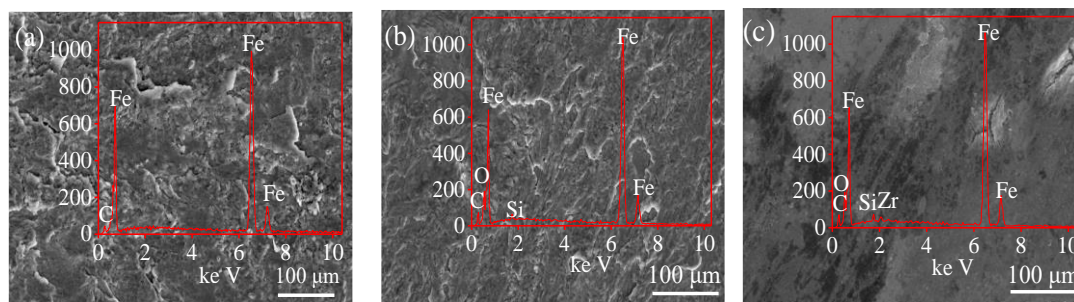
Figure 1. SEM micrographs with EDS of the samples (a) sample 1; (b) sample 2; (c) sample 3.

3.2 Structural Analysis of Salt-doped Silane Films on Metal Surface

Fig. 2(a) shows the full scan XPS spectra of sample 3. The composite film of this sample consisted mainly of Si, Zr, C, O, F, and Fe. However, sodium fluorozirconate is a strong electrolyte and, hence, a small amount of Na element remained on the surface of the film. Moreover, the XPS spectrum is unable to observe the H element [29].
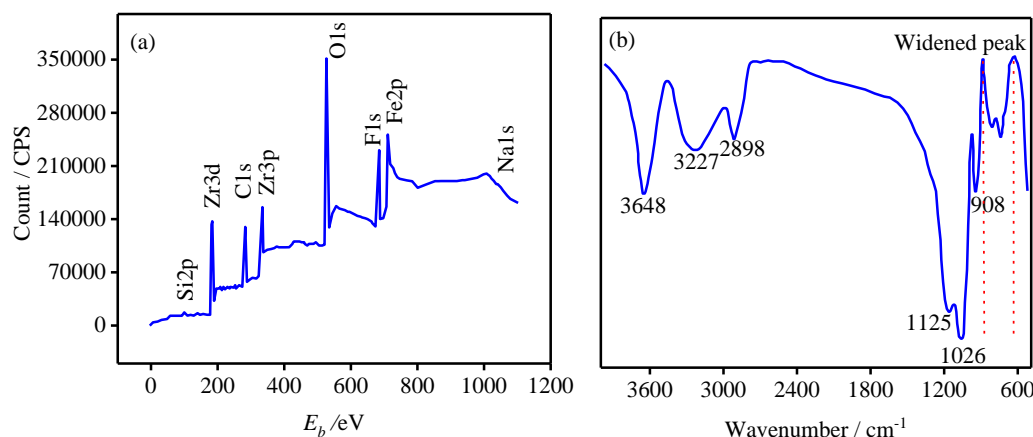
Figure 2. Full X-ray photoelectron spectroscopy (XPS) scan and infrared absorption spectrum of sample 3: (a) full scan XPS spectra; (b) infrared absorption spectrum.

Fig. 2(b) shows the infrared absorption spectrum of sample 3. The absorption peaks at 3648 cm^{-1} and 908 cm^{-1} corresponded to the -OH stretching vibration of Si—OH, indicating that Si—OH is incompletely condensed on the substrate surface, and free hydroxyl groups are present. In addition, the shoulder band at 3227 cm^{-1} can be attributed to the hydrogen bond association peak of the OH group. The absorption peak at 2898 cm^{-1} was generated by the symmetric stretching vibration of the methylene group. Similarly, the shoulder band at 1125 cm^{-1} and 1026 cm^{-1} corresponded to the absorption peak generated by the asymmetric stretching vibration of Si—O—Si. Broadening peaks occurring at 665–900 cm^{-1} resulted mainly from the overlap of Si-O-Si and Si-O-Zr absorption peaks. In other words, the surface of the fluorozirconic acid-silane composite film formed a protective film (composed mainly of Si—O—Si bonds) and a strongly cohesive valence bond with metal ions.
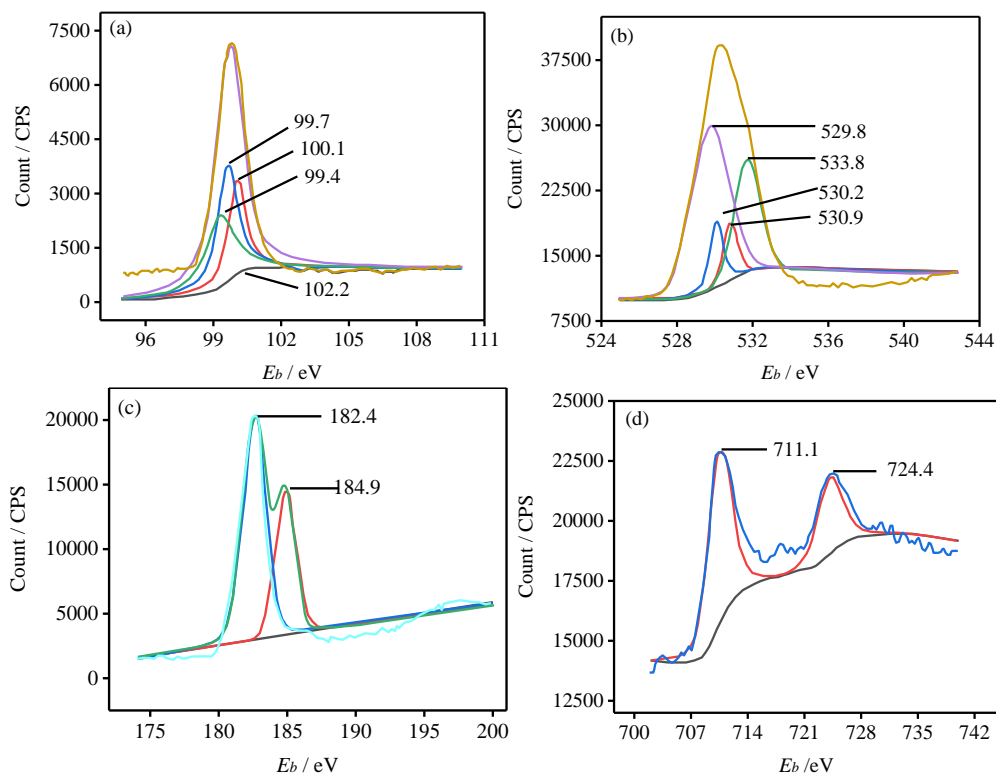
Figure 3. XPS narrow scan spectras of sample 3: (a) Si^{2p}; (b) O^{ls}; (c)Zr^{3d}; (d)Fe^{2p}.

Fig. 3 shows the XPS narrow scan spectra of the main elements (Si, O, Zr, and Fe) in sample 3. The Gauss/Laurence equation was fitted to the minimum mean square error Shirley elimination method, and the NIST Data base database was used to compare the binding energy of the fitted peaks [30]. Fig. 3(a) shows that the Si2p peak consisted of four fitted peak stacks with binding energies of 102.2, 99.7, 100.1, and 99.4 eV corresponding to Si—O—Si, Si—O—Fe, and C—Si, respectively. —O—Si—C and Si in Si—O—Zr indicated that the silane was already adsorbed on the surface of the sample and formed a three-dimensional network structure. In Fig. 3(b), the O^{ls} peak was mainly composed of four fitted peaks, with binding energies of: 533.8, 530.2, 529.8, and 530.9 eV corresponding to Si—O, Si—O—Fe, Fe—O, and O with ZrO$_2$, respectively [15]. Fig. 3(c) shows that the Zr^{3d} peak was composed of two fitted peaks. The corresponding binding energies, 18.4 and 182.4 eV, were associated with the Zr peaks in ZrO$_2$ and ZrF$_2$, respectively, indicating the presence of ZrO$_2$ in the composite film. The peak of Fe$^{2pl/2}$ for the composite film occurred at 711.1 eV, which was associated with the peak of Fe in Fe-O (see Fig. 3(d)). The peak of Fe$^{2p3/2}$ occurred at 724.4 eV, corresponding to the peak of Fe in Fe—OH (hydrate of iron). In short, the fluorozirconic acid-silane composite film formed a three-dimensional network structure on the metal surface. That is, the fluorozirconate was deposited on the surface and formed a composite film layer comprising oxides and hydroxides of Fe and Zr.

3.3 Tested and Analysis of Electrochemical Performance

Fig. 4 shows the potentiodynamic polarization curves of the samples. The polarization curves of sample 2 and (especially) sample 3 moved toward the direction of low current compared with the polarization curve of sample 1. This indicated the good anti-corrosion properties of the fluorozirconic acid-silane composite film. The composite film isolated the surface of the cold-rolled steel from the corrosive medium, thereby hindering the diffusion and migration of electrons in the electric double layer between the solution and the metal [31]. The corresponding electrochemical parameters (E_{corr}, β_a, β_c, and i_{corr}) shown in Table 1 confirmed the anti-corrosion properties of the composite film. For example, i_{corr} of sample 3 (i_{corr}= 0.223 A/cm^2) was significantly lower than that of sample 1 (i_{corr} = 0.117 A/cm^2).
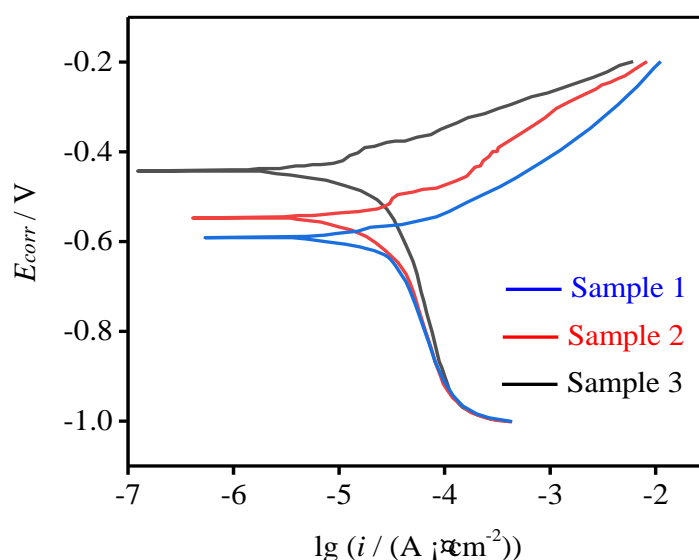
Figure 4. Potentiodynamic polarization curves (scanning rate: -1 mV/s) of the samples in 3.5 wt.% NaCl solution at 25 ± 1°C.

Table 1. Electrochemical parameters (E_{corr}, β_a and i_{corr}) obtained from potentiodynamic polarization curves in Figure 4

Sample	E_{corr} (mV)	β_a (mV dec^{-1})	i_{corr} (A cm^{-2})
sample 1	-611	81.7	0.223
sample 2	-587	128.6	0.193
sample 3	-442	249.3	0.117

In the NaCl solution, the metastable zirconia is gradually eroded into a complex-ion-based $ZrCl_6^{2-}$. During the subsequent polarization processes, anodic polarization constitutes the main polarization reaction of the ZrO_2 coating. The steps in these processes are as follows [32]:

Cathodic reaction: $ZrO_2+4H^+== Zr^{4+}+2H_2O$ (1)

Anode reaction: $ZrO_2 + 2Cl^- = ZrOCl_2 + O^{2-}$ (2)

$$ZrOCl_2 + 4Cl^- == ZrCl_6^{2-} + O^{2-}$$ (3)
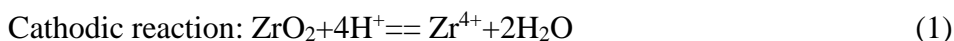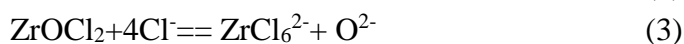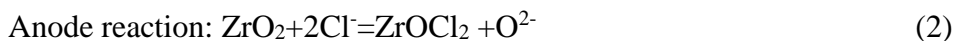
The influence of the ZrO_2-doped silane film on the anode polarization of the sample was investigated (see corresponding polarization curves in Fig. 5).
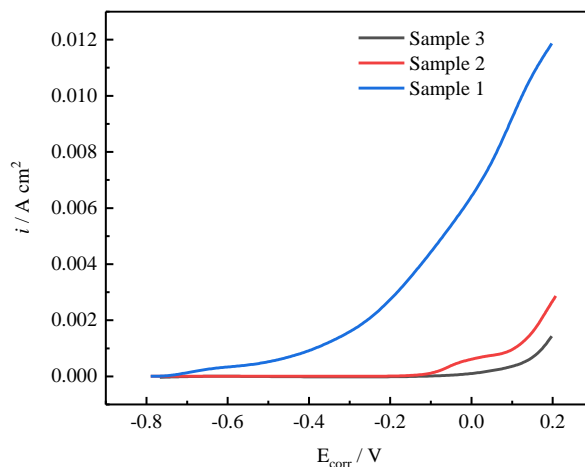
Figure 5. Anodic polarization curve (scanning rate: 0.5 mV/s) of the samples in 3.5 wt.% NaCl solution at $25 \pm 1°C$.

The current density branch of each film-coated sample was suppressed, i.e., the current densities of sample 1 and sample 3 were always smaller than that of sample 2. This indicated the corrosion resistance of the protective film. The resistance of the composite film was superior to that of the other films [33]. When the potential was increased to 0.1 V, the corrosion current density of sample 2 increased gradually, indicating that the ZrO_2 silane film started to fail and the level of corrosion increased gradually. The corrosion current density at a potential of 0.2 V remained almost unchanged for sample 3, but increased linearly for sample 2. That is, the anti-corrosion effect of the fluorozirconic acid-silane composite film was significantly better than that of the single film. The difference in the shape of these curves revealed that the ZrO_2 particles in the silane film had no effect on the dissolution process. However, this process occurred at a higher negative potential (0–0.2 V) than the potential associated with the dissolution process of sample 2 and sample 3, indicating the synergistic anti-corrosion effect of silane and ZrO_2.
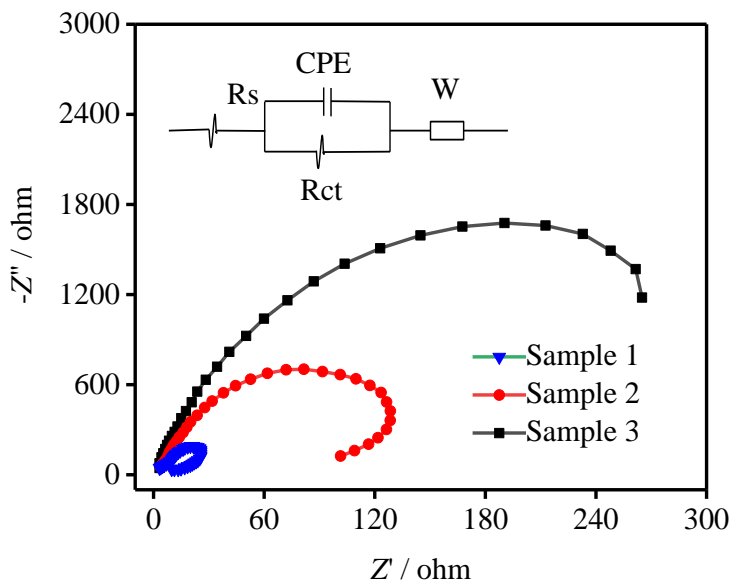
Figure 6. AC impedance spectrum and equivalent circuit diagram of the samples (AC excitation signal is 1 mV/s with 25 ± 1°C).

Fig. 6 shows a Nyquist plot consisting of the AC impedance spectrum and equivalent circuit diagram of the samples in 3.5% NaCl solution. The spectrum of each sample was characterized by a circular arc shape. However, the spectral radius of sample 3 was significantly larger than the spectral radius of the other samples, indicating that the polarization resistance was the largest. According to a previous study [34], the corrosion rate decreased with increasing polarization resistance and, hence, the composite film exhibited better corrosion resistance than the other films. This result is consistent with the polarization curve analysis. The data were fitted by using the Zsimple software (see Table 2 for the relevant parameters). The parameters R_S, R_{pf}, and R_{po}, corresponding to the solution resistance, first loop of the Nyquist plot, and pore resistance, respectively, were essential for a perfect coating. C_1 is the capacitance of the porous outer layer. R_s values of 871.3, 963.2, and 989.2 Ω were obtained for sample 1, sample 2 and sample 3, respectively.

Table 2. Fitting parameter values of equivalent circuit model in Figure 6

Sample	R_s (Ω cm^2)	R_{pf} (kΩ cm^2)	R_{po} (Ω cm^2)	C_1 (μF cm^{-2})	C_2 (μF cm^{-2})
sample1	871.3	130	250	0.223	56
sample2	963.2	131	571	0.119	59
sample3	989.2	134	670	0.017	64

3.4 Analysis of Soaking Test and Medium Salt Spray Test

The surface corrosion area of the samples changed with the immersion time in 5% NaCl solution, as shown in Fig. 7(a). Form the figure, for a given immersion time, the corrosion resistance of sample 2 and sample 3 (which are protected by the film) was significantly higher than that of sample 1. The surface corrosion area of sample 1 increased sharply and linearly during a 10-day immersion of

the sample, and reached a value of 98% within 25 days. In contrast, the corrosive area of sample 3 increased only modestly with increasing soaking time, i.e., changing from 3.5% on the 10th day to 7.5% for the 25th day. At this time, the corrosive area of sample 2 was 12.2%.
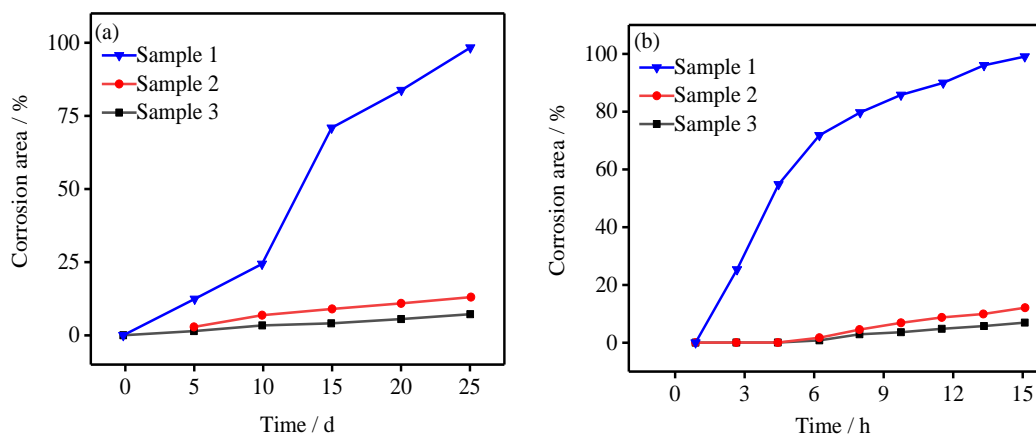
Figure 7. Changes in surface corrosion area associated with different immersion times in 5% NaCl solution (a) and results of the 15-h moderate salt spray test (b) of the samples.

During the corrosion test, the corrosion area was smallest and increased most slowly in the case of sample 3, indicating that the fluorozirconic acid-silane composite film exhibited the strongest corrosion resistance [35]. The stability of this sample in the NaCl solution was 38.5% higher than that of the silane film. A moderate salt spray test was conducted for 15 h to further explore the corrosion resistance of the protective film (see Fig. 7(b) for the test results). As shown in the figure, the silane film and composite film were effective in delaying corrosion on the surface of the cold rolled steel [36]. After 1 h in a salt spray situation, sample 1 underwent corrosion and a corrosive area corresponding to 25% of the sample area was formed. The corrosion area increased linearly and considerably with increasing time, reaching 80% after 7 h of the test, and then decreasing thereafter. Small corrosive areas formed on sample 2 and sample 3 after 7 h of the test. In 13 h of the salt spray test, corrosive areas of 96%, 8%, and 5% formed on sample 1, sample 2, and sample 3, respectively. These results indicated that the corrosion resistance of sample 3 was significantly higher than that of sample 1. sample 2 and sample 3 exhibited excellent short-term corrosion resistance, but the growth rate of the corrosion area occurring on sample 3 was lower than that of sample 2. Therefore, the stability and corrosion resistance of sample 3 were greater than that of sample 2[37]. In summary, the fluorozirconic acid-silane composite film exhibited better corrosion resistance than the silane film, which is consistent with the immersion test results performed in 5% NaCl solution.

The corrosion resistance of the ZrO_2-doped silane film prepared in this work was considerably larger than that of ZrO_2-doped silane films reported in the literature, as shown in Table 3. The E_{corr} and i_{corr} of the passivator considered in the present work are superior to those of the ZrO_2-doped silane films reported in the literature, indicating the remarkable corrosion-resistance ability of the present film.

Table3. Corrosion potential (E_{corr}) and corrosion current density (i_{corr}) of the samples obtained via different methods.

ZrO$_2$-doped film	E_{corr} (mV)	i_{corr} (A cm^{-2})
ZrO$_2$-based sol-gel films [38]	-510	0.550
Zn–ZrO$_2$ composite coatings[39]	-1028	0.119
hydroxyapatite/zirconia composite coating [40]	-582	0.398
Ni–ZrO$_2$ composite coatings[41]	-477	0.431
This work	-442	0.117

4. CONCLUSIONS

1) Using a sol-gel method, a fluorozirconic acid-silane composite film was successfully prepared on the surface of a cold-rolled steel sheet.

2) The corrosion current of the fluorozirconic acid-silane composite film was 10% lower than that of the monosilane film, and the corrosion resistance was remarkably improved. Furthermore, the stability of the composite film subjected to a 25-day sodium chloride solution immersion test was 38.5% higher than that of the silane film.

3) The Si-0-Zr bond formed by the composite film can improve the bonding force between the film and the metal substrate, thereby improving the corrosion resistance of the silane film.

References

1. X.C. Wang, Q. Yang, X.Z. Du, Z.Y. Jiang, *Int. J. Min. Met. Mater.*, 17(2010) 5.
2. B. Ramezanzadeh, M.M. Attar, *J. Coat. Technol. Res*., 10(2013) 1.
3. Y. Kim, J. Lee, J.H. Oh, *Microelectron. Eng.*, 191(2018) 23.
4. Z.H. Cai, H.Y. Li, S.Y. Jing, Z.C. Li, H. Ding, Z.Y. Tang, R.D.K. Misra, *Mater. Charact.*, (2018) 137.
5. Y.N. Singhbabu, B. Sivakumar, S.K. Choudhary, S. Das, R.K. Sahu, *Surf. Coat. Tech.*, (2018) 349.
6. R. Yan, W. He, T.R. Zhai, H. Ma, *Appl. Surf. Sci.*, (2018) 442.
7. M.A. Shuang, D.E.N.G. Yue, W.U. Wen, T.A.N. Yu, N.A. Li, S.U.N. Panpan, *Chin. Soc. Corros. Prot.*, 36 (2016) 4.
8. X. Li, H. Chen, P. Chen, C.X. Qing, H. Li, *J. Mater. Eng. Perform.*, 26 (2017) 5.
9. L.Y. Cui, P.H. Qin, X.L. Huang, Z.Z. Yin, R.C. Zeng, S.Q. Li, Z.L Wang, *Surf. Coat. Tech.*, (2017) 324, 560-568.
10. N. Ramdani, M. Derradji, J. Wang, W.B. Liu, E.O. Mokhnache, *Plast. Rubber Compos.*, *45* (2016) 2.

11. A. Atiqah, M. Jawaid, M.R. Ishak, S.M. Sapuan, *J. Nat. Fibers*, 15 (2018) 2.
12. A. Petcherdchoo, *Adv. Mater. Res.*, (2014) 931.
13. S. Akhtar, A. Matin, A.M. Kumar, A. Ibrahim, T. Laoui, *Appl. Surf. Sci.*, (2018) 440.
14. S. S. Pathak, A. S. Khanna, *Prog. Org. Coat.*, 65 (2009) 2.
15. J. Wojciechowski, K. Szubert, R. Peipmann, M. Fritz, U. Schmidt, A. Bund, G. Lota, *Electrochim. Acta*, (2016) 220.
16. M. Khayet, J.P.G. Villaluenga, J.L. Valentin, M.A. López-Manchado, J.I. Mengual, *Polymer*, 46 (2005) 23.
17. C. Chen, S. Dong, R. Hou, J. Hu, P.X. Jiang, C. Ye, C.S. Lin, *Surf. Coat. Tech.*, (2017) 326.
18. K.J. Jothi, K. Palanivelu, *Appl. Surf. Sci.*, 13 (2014) 288, 60-68.
19. M.F. Montemor, R. Pinto, M.G.S. Ferreira, *Electrochim. Acta*, 54 (2009) 22.
20. P.R. Varma, J. Colreavy, J. Cassidy, M. Oubaha, C. McDonagh, B. Duffy, *Thin Solid Films*, 518 (2010) 20.
21. E. Ramanathan, S. Balasubramanian, *Surf. Coat. Tech.*, (2016) 304.
22. P. Taheri, K. Lill, J.H.W. DeWit, J.M.C. Mol, H. Terryn, *J. Phys. Chem. C*, 116 (2012) 15.
23. E. Almeida, *Ind. Eng. Chem.*, 20 (2001) 1.
24. P. Puomi, H. Fagerholm, J. Rosenholm, K. Jyrkäs, *Surf. Coat. Tech.*, 115 (1999) 70.
25. O. Awadallah, Z. Cheng, *Sol. Energ. Mat. Sol. C.*, 12 (2018) 176.
26. G.E. Della, E. Menin, G. Maggioni, C. Sada, A. Martucci, *Materials*, 11 (2018) 3.
27. S.W. Han, I.H. Kim, J.H. Kim, H.O. Seo, Y.D. Kim, *Polymer*, (2018) 138.
28. Z.W. Zhao, G. Zhang, H.G. Li, *J. Cent. South. Univ. T.*, 11 (2004) 2.
29. P. Laha, T. Schram, H. Terryn, *Surf. Interface Anal.*, 34 (2002) 1.
30. R. Matsumoto, Y. Nishizawa, N. Kataoka, H. Tanaka, H. Yoshikawa, S. Tanuma, K. Yoshihara, *J. Electron Spectrosc.*, 12 (2016) 207.
31. S.S. Vinogradov, S.V. Balakhonov, S.A. Demin, O.G. Kirillova, *Prot. Met. Phys. Chem.*, 53 (2017) 7.
32. Z. Lei, Q. Zhang, X. Zhu, D. Ma, F. Ma, Z. Song, Y.Q. Fu, *Appl. Surf. Sci.*, (2018) 431.
33. A. Bao, J. Zhu, W. Liu, *Hot Work. Tech.*, 49 (2015) 8.
34. Y. Dun, X. Zhao, Y. Tang, S. Dino, Y. Zuo, *Appl. Surf. Sci.*, (2018) 437.
35. D. Thirumalaikumarasamy, K. Shanmugam, V. Balasubramanian, *J. Asian. Ceram. Soc.*, 2 (2014) 4.
36. Y. Wu, S. Zhu, P. Shi, B. Yan, D.Z. Cai, Y.A. Zhang, *Rsc Adv.*, 7 (2017) 25.
37. J. Zhang, B. Meng, X. Wang, W. Li, *High Temp. Mat. Pr-Isr.*, 36 (2017) 1.
38. Z.U.O. Ke, W.A.N.G. Xin, L.I.U. Wei, Z. Yue, *T. Nonferr. Metal. Soc.*, 24 (2014) 5.
39. K. Vathsala, T.V. Venkatesha, *Appl. Surf. Sci.*, 257 (2011) 21.
40. D. Qiu, A. Wang, Y. Yin, *Appl. Surf. Sci.*, 257 (2010) 5.
41. R. Arghavanian, N.A. Parvini, *Surf. Eng.*, 27 (2011) 9.